PCCP

2D Auxetic Material with Intrinsic Ferromagnetism: Copper Halide ($CuCl_2$) Monolayer

Journal:	*Physical Chemistry Chemical Physics*
Manuscript ID	CP-ART-06-2021-002834.R1
Article Type:	Paper
Date Submitted by the Author:	25-Aug-2021
Complete List of Authors:	Qin, Haifei; Southwest Jiaotong University, School of Physical Science and Technology Chen, Jiao; Southwest Jiaotong University, School of Physical Science and Technology Sun, Bai; Southwest Jiaotong University, School of Physical Science and Technology Tang, Yongliang; Southwest Jiaotong University, Physical Science and Technology Ni, Yuxiang; Southwest Jiaotong University, School of Physical Science and Technology Chen, Zhongfang; University of Puerto Rico, Department of Chemistry Wang, Hongyan; Southwest Jiaotong University, ; Chen, Yuanzheng; Southwest Jiaotong University, School of Physical Science and Technology

2D Auxetic Material with Intrinsic Ferromagnetism: Copper Halide ($CuCl_2$) Monolayer

Haifei Qin,[a] Jiao Chen,[a] Bai Sun,[a] Yongliang Tang,[a] Yuxiang Ni,[a] Zhongfang Chen,[b,*]
Hongyan Wang,[a] Yuanzheng Chen[a, c, d, *]

[a] *School of Physical Science and Technology, Key Laboratory of Advanced Technologies of Materials, Ministry of Education of China, Southwest Jiaotong University, Chengdu 610031, China*

[b] *Department of Chemistry, University of Puerto Rico, Rio Piedras Campus, San Juan, PR 00931, USA*

[c] *Beijing Computational Science Research Center, Haidian District, Beijing 100193, China*

[d] *Department of Physics and Centre for Advanced Two-Dimensional Materials, National University of Singapore, Singapore 117551, Singapore.*

Abstract:

The discovery of ferromagnetism in monolayer transition metal halides exemplified by CrI_3 has opened a new venue in the field of two-dimensional (2D) magnetic materials, and more such 2D materials are awaiting explorations. Herein, by means of swarm-intelligence global minimum structure-searching methods in conjunction with first principles calculations, we identified a novel $CuCl_2$ monolayer which exhibits not only intrinsic ferromagnetism but also auxetic mechanical property originating from the interplay of lattice and Cu-Cl tetrahedron symmetries. The predicted Curie temperature of $CuCl_2$ reaches ~47 K, and its ferromagnetism is associated with the strong hybridization between Cu 3*d* states and Cl 3*p* states in the configuration. Moreover, upon a biaxial tensile strain or carrier doping, the $CuCl_2$ monolayer can be converted from ferromagnetic to nonmagnetic as well as from half-metal to metal. These properties endow this $CuCl_2$ monolayer with great potential for applications in auxetic/spintronic nanodevices.

Keywords: Magnetic materials; Copper Halide Monolayer; Negative Poisson's ratio; Structure design, first principles calculations

1. Introduction

According to the Mermin-Wagner theorem, in theory, long-range magnetic order at finite temperature is prohibited in two-dimensional (2D) Heisenberg spin systems.[1] Thus, the ferromagnetism (FM) had long been absent among 2D systems until the recent breakthroughs in finding intrinsic FM in atomically thin CrI_3,[2] Fe_3GeTe_2[3] and $Cr_2Ge_2Te_6$.[4] In the experiments, $Cr_2Ge_2Te_6$ was exfoliated down to a bilayer with Curie temperature Tc of 28 K, while the

monolayers of CrI_3 and Fe_3GeTe_2 were obtained with Tc of 45 K and 68 K, respectively. These discoveries have sparked intense interest and inspired extensive research about 2D FMs, due to their great potential for nanoscale device applications, such as spin valves, spin filters, and data storage.[5]

Before the discovery of intrinsic 2D FMs, various methods were developed to induce magnetism into 2D systems, such as strain engineering,[6, 7] carrier doping,[8-10] adsorption,[11, 12] and chemical functionalization.[13, 14] Notably, recent theoretical studies predicted that doping the 3*d* transition-metals (V, Mn, Fe, Co, Ni, Cu, and Zn) can bring magnetism to the MoS_2 monolayer,[15] what particularly interesting is that even though Cu is a nonmagnetic dopant, the Cu-doped system shows unexpectedly strong magnetism because of the strong hybridization between Cu 3*d* states and S 3*p* states. Similarly, a layered antiferromagnetic (AFM) structure based on 2D CuO_2 planes was predicted, and its AFM state correlates with its Cu 3*d* configuration and a large degree of *p-d* hybridization.[16, 17] Moreover, an AFM state in the 1D chain-like CuF_2 and $CuCl_2$ compounds were reported,[18, 19] and single-layers of K_2CuF_4 were predicted to be ferromagnetic 2D crystals.[20] These findings proved the possibility to realize ferromagnetic states in the Cu-based compounds.

Since the discovery of the ferromagnetic order in 2D CrI_3, several other transition metal halides AB_x (A = metal cation, B = halogen anion, x = 2 or 3) monolayers, such as $FeCl_2$,[21] $CoBr_2$,[22] $CrCl_3$,[23] $CrBr_3$[24] and VI_3,[25] have been theoretically investigated. Depending on the numbers of 3*d* electrons in the transition metal atom and the strength of halides crystal fields, these transition metal halides exhibit distinct electronic and magnetic properties. Very recently, Gao *et al.* predicted that 2D CuCl crystal can be multiferroic under ambient conditions with coupled ferroelectricity and ferroelasticity.[26] These discoveries indicate a strong likelihood of the existence of 2D intrinsic FM among Cu-based halide, which inspired us to explore 2D FM in Cu-Cl system.

Herein, by means of a crystal structure search algorithm in conjunction with density functional theory (DFT) calculations, we systematically investigated 2D Cu-Cl systems. As expected, we successfully identified a novel $CuCl_2$ monolayer with intrinsic FM. Meanwhile, we found that this monolayer is an auxetic material, as evidenced by its ultrahigh absolute value (~0.4) of negative Poisson's ratio (NPR). In addition, applying the tensile/compressive strain and carrier doping can further tune its magnetic and electronic properties, leading to a transformation of ferromagnetic → nonmagnetic and half-metal → metal. These unique properties endow the $CuCl_2$ monolayer as a promising candidate for many advanced applications in spintronics and multifunctional devices.

2. Computational Methods

The crystal structure search algorithm of particle swarm optimization (PSO) method, as implemented in the CALYPSO code,[27-29] was employed to search stable structures of 2D Cu-Cl and Cu_xCl_{1-x} (x=2/3, 1/2, 3/7, 2/5, 1/3, 1/4, 1/5) monolayers. The effectiveness and efficiency of the PSO method have been well proven on various systems and compounds.[30-39] We adopted a vacuum distance greater than 15 Å in the *z* direction to eliminate the interactions between adjacent layers.[40] Spin-polarized density functional theory (DFT) computations were performed using the VASP code[41] for geometry optimizations and electronic structure calculations, and the exchange-correlation functional was described by the Perdew-Burke-Ernzerhof (PBE) functional within the generalized gradient approximation (GGA)[42] unless mentioned otherwise. The electron projector augmented wave (PAW) [43, 44] potentials of Cu and Cl treat $3d^{10}4s^1$ and $3s^23p^5$ electrons as the valence electrons, respectively. The GGA+U approach was also adopted for the 3*d* orbitals of the transition metal Cu, and the Heyd−Scuseria−Ernzerhof (HSE06) hybrid function[45] was used to more accurately describe the bandgap. The cut-off energy is set to 800 eV, and the Brillouin zone is sampled with a resolution of $2\pi \times 0.025$ Å^{-1} using the Monkhorst−Pack method.[46] The energy convergence threshold and the force convergence criteria were set as 1×10^{-6} eV and 0.01 eV/Å, respectively. Phonon dispersion calculations were carried out by a supercell approach using the Phonopy code.[47] To evaluate the thermal stability, ab initio molecular dynamics (AIMD) simulations are performed with a 6×6×1 supercell at 300 K with a canonical ensemble (NVT).[48] Carrier doping was performed by adding or removing electrons from the unit cell in the periodic boundary conditions computations, in which the system was neutralized by a uniform charge background. The Monte Carlo simulations based on the Heisenberg model were employed to describe the thermal dynamics of magnetism in equilibrium states,[49, 50] for which the open source project MCSOLVER code was used.[51] The details about our structural search procedure and computational methods are given in the Supporting Information.

3 Results and Discussion

3.1. Crystal structure, stability, and electronic properties

After a global structure search at various Cu/Cl ratios in the Cu_xCl_{1-x} ($0<x<1$) compositions, we identified the 2D crystal phases at each composition and computed their energies to determine the most viable structure. To evaluate their relative thermodynamic stability, we further calculated their formation energies and constructed the convex hull (Fig. S1), defined as $\Delta E(Cu_{1-x}Cl_x) = E(Cu_{1-x}Cl_x) - (1 - x)E(Cu) - xE(Cl)$. Several energetically stable Cu-Cl compositions (e.g., Cu_2Cl, CuCl, $CuCl_2$, $CuCl_3$) are located on the line of convex hull,

and their $Cu_{1-x}Cl_x$ monolayers have been obtained as shown in Fig. S2. Notably, this exercise leads to a discovery of intrinsic FM in a Cl-rich $CuCl_2$ monolayer, which is the focus of this work.

The $CuCl_2$ monolayer adopts a tetragonal structure [space group *P*-4/*m*2, one formula unit (Fig. 1a)], in which each Cu atom connects with four Cl atoms, and each Cl atom bonds with two Cu atoms, forming a $CuCl_4$-tetrahedron with only one uniform length of Cu-Cl bond, and consequently, no atom has redundant valence electrons. The detailed crystal structural parameters are summarized in Table S1. In the top view, the $CuCl_2$ monolayer has a rectangular crystal configuration with inherent –Cu–Cl–Cu–bucklings and strong symmetry in the *a*−*b* plane, which is very similar to the δ-2D SiO_2 phase.[52] The Cu-Cl distance (2.257 Å) is larger than the sum (1.95 Å) of covalent radii of Cu and Cl atoms, indicating the formation of noncovalent Cu−Cl bonds. The electron localization function (ELF) analysis (Fig. 1b) reveals the charge fluctuation and thus a strong ionic feature for these Cu−Cl bonds.

To assess the dynamic stability of our predicted $CuCl_2$ monolayer, we calculated its phonon dispersion curves (Fig. 1c) using the finite-displacement method. The absence of any significant imaginary modes in the first Brillouin zone demonstrates its dynamic stability. By performing AIMD simulations in the canonical ensemble, its thermal stability was evaluated at 300 K. It is found that the $CuCl_2$ monolayer well maintains its structural integrity (Fig. 1d), and only slight deformation occurs after a simulation of 5 ps, which indicates its good thermal stability at normal conditions. Moreover, we also examined the mechanical stability of the $CuCl_2$ monolayer by calculating its elastic constants. The elastic constants obtained by the strain-energy method are C_{11} = 14.71, C_{22} = -5.82, C_{12} = 14.71, and C_{66} = 1.94 N/m, respectively. Clearly, the Born−Huang criteria[2] for a mechanically stable 2D material (e.g., *i.e.*, $C_{11} > C_{12}$, $C_{11}C_{22} - C_{12}^2 > 0$, $C_{66} > 0$) can be satisfied in the $CuCl_2$ monolayer, indicating its mechanical stability.

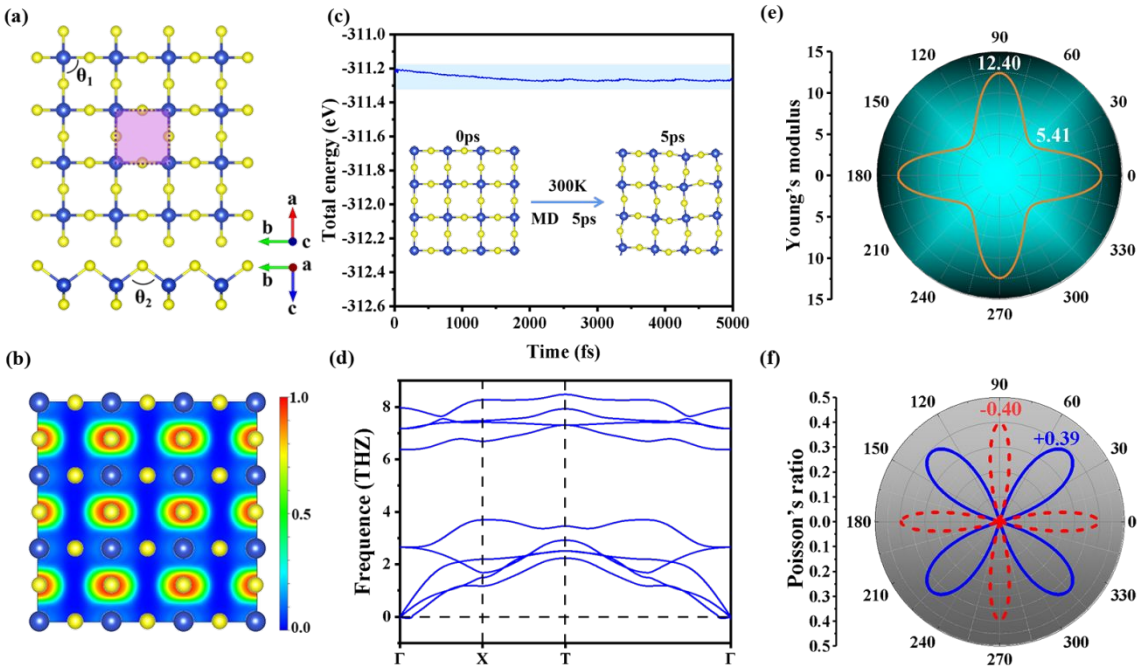

Fig. 1. The structure symmetry of (a) $CuCl_2$ monolayer from the side and top views. The yellow and blue atoms represent Cl and Cu atoms. (b) Electron localization function map of the $CuCl_2$ monolayer. (c) The structure and total-energy evolution for $CuCl_2$ monolayer in AIMD simulations at T = 300 K for 5 ps (d) Phonon dispersion curves of $CuCl_2$ monolayer. The Poisson's ratio (e) and Young's modulus (f) of $CuCl_2$ monolayer, the solid blue line, and the imaginary red line represent the positive and negative values.

To examine the mechanical behaviors of the $CuCl_2$ monolayer, we further calculated its in-plane Young's modulus Y(θ) and in-plane Poisson's ratio υ(θ) based on the elastic constants. As shown in Fig. 1e-1f, Young's modulus Y(θ) and Poisson's ratio υ(θ) of the $CuCl_2$ monolayer both exhibit strong anisotropy, implying different mechanical responses against the same strain along different directions. The highest value of Young's modulus is 12.40 N/m at θ = 90° and 270°, which is much smaller than that of MoS_2 (129 N m^{-1})[53] and BN (318 N m^{-1}).[54] This relatively low Young's modulus endows $CuCl_2$ a potential mechanic flexibility. Interestingly, an obvious NPR is obtained in the $CuCl_2$ monolayer along its *x*, *y* directions and neighboring directions (Fig. 1f). The $CuCl_2$ monolayer in both *x*- and *y*-directions have a large NPR value of −0.40. This absolute value of NPR is quite high, larger than δ-phosphorene (-0.267)[55] and Ag_2S (-0.12),[56] and is comparable to those of W_2C (-0.4),[57]SiSe (-0.413),[58] and PtI_2 (-0.54).[59]

As we know, materials with NPR also called auxetic materials, which have unique properties that they could expand when stretched or laterally shrink when compressed. Thus the calculated NPR results indicate that the $CuCl_2$ monolayer is an auxetic material, which originates from a

coupling of lattice symmetry and Cu−Cl tetrahedron symmetry. As discussed above, $CuCl_4$-tetrahedron is the basic unit in the structure of $CuCl_2$ monolayer. In particular, the $CuCl_4$-tetrahedron of symmetry group T_d has one special orthogonal projection, which goes through on opposite edges (2-fold axis).[52] For the $CuCl_2$ monolayer, the lattice vector is along the 2-fold axis, which means the distance of two Cl atoms will increase when the tensile strain is applied to the edge to the tetrahedron (as shown in Fig. S3), giving rise to the appearance of NPR. A similar mechanism of NPR has been found in 2D Si-O crystals.[52]

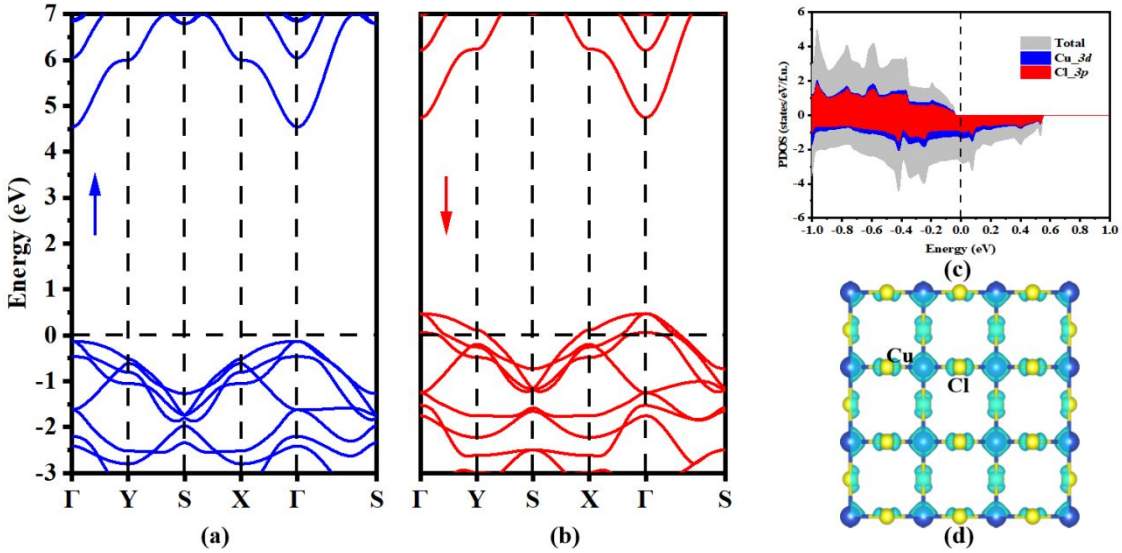

Fig. 2. The spin band structures of $CuCl_2$ monolayer of spin up (a) and spin down (b) state with HSE06 function. The blue line and red line represent the spin up and spin down, respectively. (c) The spin PDOS of Cu 3*d* and Cl 3*p* orbitals in the $CuCl_2$ monolayer, and (d) the spin-charge density distribution of $CuCl_2$ monolayer with an isosurface value of 0.009 a.u.

3.2. Magnetic and electronic properties

To explore the magnetic properties of the $CuCl_2$ monolayer for applications in nanoelectronics, we firstly identified its ground state by computing energies in both spin-polarized and unpolarized cases using the standard GGA functional. It is found that the ground state of $CuCl_2$ is spin-polarized, exhibiting intrinsic FM. Considering the valence electron of Cu is from a 3*d* orbital in the magnetic calculations, it is essential to examine the influence of Hubbard U correction.[60, 61] Thus, we further performed GGA+U calculations to examine the relative energies of different states including nomagnetism (NM), ferromagnetism (FM), antiferromagnetism (AFM), as well as the lattice constants, magnetic moments, and spin-polarized band structures of the $CuCl_2$ monolayer. Regardless of the used U_{eff} value (in the range of 0~3 eV), the FM configure is always of the lowest energy (Fig. S4), indicating that the FM is the ground state of $CuCl_2$ monolayer at GGA+U level of theory, the same as that

obtained by PBE computations. Moreover, compared with PBE results, the lattice constants, magnetic moment, and spin-polarized band structures of the $CuCl_2$ monolayer all have no obvious change after including the Hubbard U correction with different U_{eff} values (Fig. S5-S7). On the other hand, it is well known that GGA tends to underestimate the band gaps, and the hybrid exchange-correlation functional, HSE06,[43] typically gives more accurate band gap energies. Thus, we also calculated the spin-up/-down band structures of the $CuCl_2$ monolayer using spin-polarized HSE06 functional (Fig. 2a-2b). The spin-up channel is semiconducting with a wide gap of 4.67 eV at HSE06 level (~4.40 eV at the PBE level), while the spin-down channel features the metallic character with a 100% spin-polarization. Note that HSE06 reveals the same half-metal feature as obtained by PBE and GGA+U computations (Fig. S6 and S7). These above results suggest that including a Hubbard U potential functional do not have significant effect for the magnetic calculation of the $CuCl_2$ monolayer, thus standard GGA will be used in the following magnetic studies.

Analyzing the projected density of states (PDOS) (Fig. 2c) reveals that the density of states near the VBM is mainly composed of Cu 3*d* and Cl 3*p* orbitals. To assess the distribution of magnetic moments, we calculated the spin density distributions of the $CuCl_2$ monolayer (Fig. 2d) and found that the magnetism in this monolayer stems from both Cu and Cl atoms. Specifically, the magnetic moments are mostly located on the Cu atoms (~0.47 μB), with smaller contributions from each Cl atom (0.14~0.35 μB). This situation is different from the magnetism in other transition-metal halides such as CrX_3 (X = Cl, Br, I) [62] monolayers, where the magnetism arises solely from transition-metal atoms.

Moreover, we computed the Curie temperature (T_c) to estimate the effect of temperature on magnetism by using Monte Carlo simulations, Which is defined as $H = -\sum_{i,j} J_{i,j} M_i \cdot M_j$, where $J_{i,j}$ is the nearest-neighboring exchange parameter and M is the spin magnetic moment.[63] In this Monte Carlo simulations, the parameter J is estimated to be about 7.20 meV for the $CuCl_2$ monolayer. Fig. 3a summarizes the simulated magnetic moment curves and specific heat (C_v). By observing the peak position in the specific heat C_v (T) plot, the Curie temperature of $CuCl_2$ monolayer is determined to be 47 K. Under strain and carrier doping (as discussion later), the curie temperature of $CuCl_2$ monolayer is nearly unchanged.

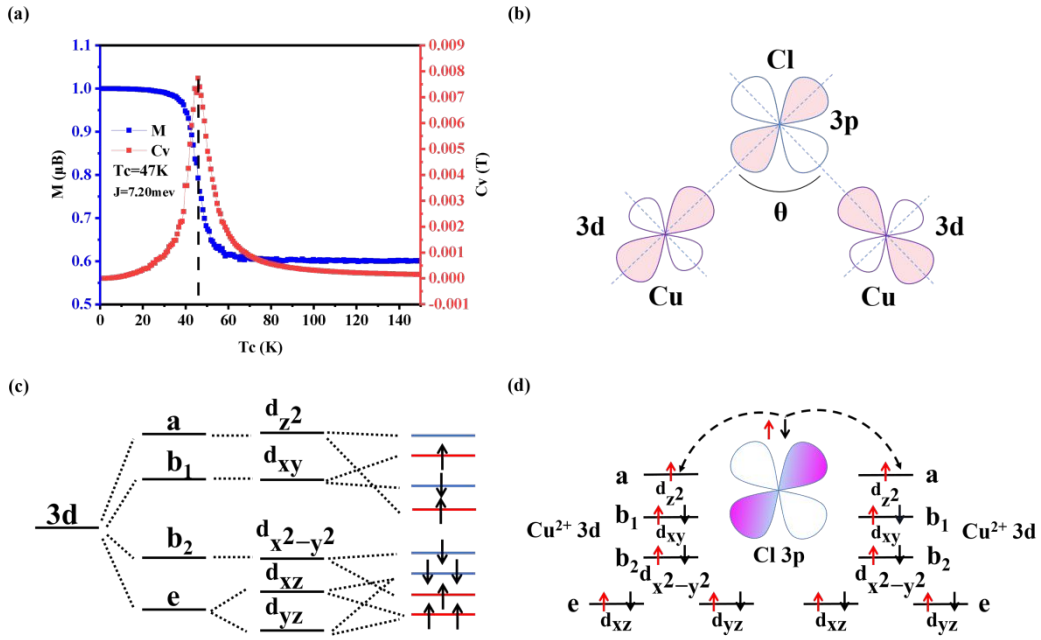

Fig. 3. (a) The magnetic moment (M) (blue) and specific heat (Cv) (red) with respect to temperature for the 2D $CuCl_2$ crystal. (b) The Cu–Cl–Cu superexchange interaction for a 90° Cu–Cl–Cu bond angle between Cu 3*d* orbital and Cl 3*p* orbital. Schematic representation of Cu-*3d* orbital splitting (c) and superexchange in the crystal field (d) of $CuCl_2$ monolayer.

The magnetism in the $CuCl_2$ monolayer can be understood from crystal field theory.[64-67] In the $CuCl_2$ monolayer, the Cu atom donates electrons to Cl atom, and the coordination of Cl atom is relatively weak, causing a high-spin configuration, and therefore the arrangement of electrons is localized on Cu^{2+}. Referring to the Cu-3*d* orbital projected density of states (Fig. S8) and crystal symmetry in the $CuCl_2$ monolayer, we obtained its schematic orbital splitting as shown in Fig. 3c. In the coordination field of 2D $CuCl_2$ crystal (D_{2d}), Cu-3*d* states split into a group of lower-energy orbitals, namely single b_2 ($d_{x^2-y^2}$) orbital and 2-fold degenerate *e* (d_{xz}, d_{yz}) orbital, and a group of higher-energy orbitals, namely single b_1 (d_{xy}) orbital and single *a* (d_{z^2}) orbital. In this coordination, according to Hund's rule,[68] when electrons are distributed to the energy degenerate orbitals, they occupy different orbitals with the same spin preference. Thus, the nine *d* electrons of Cu^{2+} ion (d^9) fully occupy the *e*, b_2, b_1 orbitals, and singly occupy the spin-up channel of *a* orbitals, while the spin-down channel of the *a* orbital is empty, resulting in an on-site magnetic moment of the Cu atom (Fig. 3d)

On the other hand, macroscopically, the energetically more favorable FM ordering of $CuCl_2$ monolayer can be understood by the Goodenough–Kanamori–Anderson (GKA) formalism.[68-70] There are two competitive distinct mechanisms that determine the magnetic ordering: (i) the direct exchange between two nearest Cu atoms (J_D) when $J_D<0$, the material is in AFM

coupling, and (ii) the chlorine-mediated Cu-Cl-Cu superexchange interaction (J_S) *via* Cl *p* states. J_S>0 is for the FM coupling. In the $CuCl_2$ monolayer, the nearest Cu-Cu distance is 3.62 Å, and their direct interaction is weak because of the large distance. In such systems with near-90° anion-mediated Cu-Cl-Cu bond angles (θ=106.8°, Fig 3b), the superexchange interaction between Cu-Cl-Cu atoms overwhelmingly results in the FM coupling.

At the micro level, the *p-d* hybridization, *i.e.*, the *d*-orbitals on adjacent Cu atoms overlapping Cl *p* orbitals, in the $CuCl_2$ monolayer is confirmed by the PDOS (Fig. 2c). The Cu-Cl-Cu superexchange interaction tuned by the Cl anion is derived from the strong *p-d* hybridization between Cl 3*p* and Cu 3*d* orbitals. More precisely, in the $CuCl_2$ monolayer, the Cl atom connecting the nearest contiguous Cu^{2+} ions distributes its spin-down electron to the unoccupied *a* (d_{z^2}) spin-down orbital of Cu^{2+}, forming a strong superexchange interaction, which results in FM. In short, the FM of $CuCl_2$ correlates with Cu 3*d* configuration and strong hybridization between Cu 3*d* states and Cl 3*p* states.

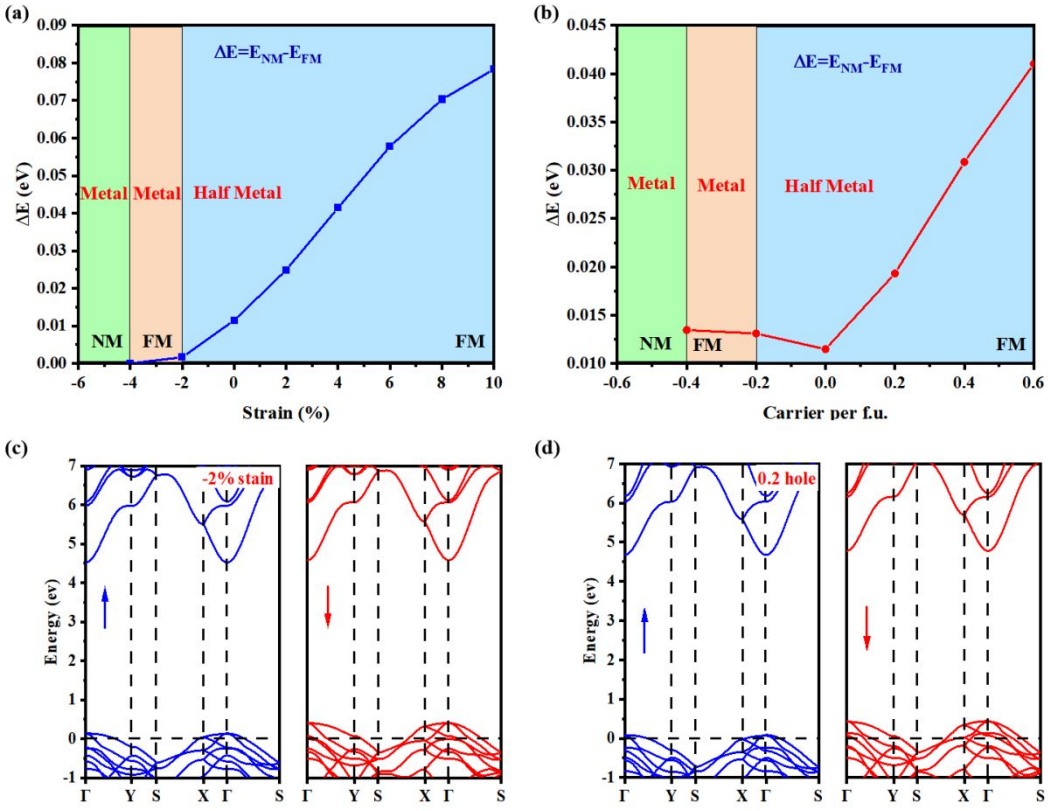

Fig. 4. (a) Strain and (b) carrier dependence of the exchange energy ΔE ($\Delta E = E_{FM} - E_{NM}$, where E_{FM} and E_{NM} are the total energy of FM state and NM states, respectively) of $CuCl_2$ monolayer. The spin band structure of (c) 2% compress strain and (d) 0.2 hole doped $CuCl_2$ monolayer. The blue line and red line represent the spin up and spin down, respectively.

3.3. Effect of strain and carrier doping on magnetic and electronic properties

Usually, such as Cr–trihalide Janus monolayers and $CoBr_2$,[71] applying strain engineering and carrier doping can tune a magnetic property of material.[65-66] Thus, we applied the in-plane biaxial strain and carrier doping to the $CuCl_2$ monolayer and examined their effects on the magnetic properties. As shown in Fig. 4a, it is found that the $CuCl_2$ monolayer can convert from FM state to NM state when the compressive strain reaches up to 2%. Similarly, the NM state is tuned to appear under the carrier doping levels up to -0.4 per f.u. (Fig. 4b). The observed change from FM state to NM state can be understood by the Stoner Criterion. According to this criterion, when the relative gain in exchange interaction is larger than the loss in kinetic energy, a spontaneous magnetism can occur when it satisfies the "Stoner Criterion": $D(E_f)J > 1$, in which the $D(E_f)$ and J represent the DOS at the Fermi energy E_f and the strength of the exchange interaction.[72, 73] In the $CuCl_2$ monolayer, when the compressive strain reaches above 4%, the variable $D(E_f)$ could not keep meeting the requirement for $D(E_f)J > 1$, giving rise to the disappearance of its FM.

Further, the change of magnetic moment was estimated at different strain strength or doping levels (Fig. S9a). When the tensile strain is applied, the total magnetic moment of the $CuCl_2$ monolayer first increases from 1.55 μB to 2 μB but remains nearly unchanged after the strain reaches to 6%. In contrast, the total magnetic moment in the case of carrier doping has no obvious change. In general, the changes of both Cu-Cu distances and Cu-Cl-Cu angles increase with aggrandizing the tensile strain (Fig. S9b). Under tensile strain, the Cu atom has a filled *d*-shell and the spatial hybridization between Cu atoms is small, resulting in a relatively low direct exchange interaction. Consequently, the influence of Cu-Cu distances is larger than Cu-Cl-Cu angles under tensile strain, thus the Cu-Cl-Cu superexchange interaction would be enhanced, leading to the increase of FM state. In the different hole-doping levels, the variations of Cu-Cu distance and Cu-Cl-Cu angle are almost unchanged, and the magnetism nearly remains the same. In contrast, with the increase of electron concentration, the Cu-Cu distances are augmented gradually, which is beneficial to FM state (Fig. S9c). Meanwhile, since the magnetic moment is mainly contributed by Cu atoms (as shown in Fig. S9a), under the strain of -2% to 4%, there is a slight improvement of magnetic moments (1-2 μB); however, under carrier doping, the magnetic is nearly unchanged. This discrepancy may be ascribed to the following difference: strain can enhance the spin splitting of Cu 3*d* orbital near the Fermi level, while carrier doping has no obvious influence (Fig. S10).

In addition, adopting the biaxial strain and carrier doping can also tune the electronic property of the $CuCl_2$ monolayer. As shown in Fig. 4c, the metallic $CuCl_2$ monolayer can

convert to a half-metal under a compressive strain of 2%. Meanwhile, under doping 0.2 hole, a similar change from half-metal to metal also occurs (as shown in Fig. 4d). Under the tensile strain and electron doping, $CuCl_2$ monolayer can still keep half-metallic.

Based on the above DFT calculations, we found that the $CuCl_2$ monolayer is a novel 2D auxetic material coupled with intrinsic ferromagnetism, thereby endowing it with potential for applications in nano multifunctional devices. Due to the non-conventional auxetic feature, the $CuCl_2$ monolayer can expand when stretched or laterally shrink when compressed, which allow them to be used in sensors, aerospace, and biomedical area. Additionally, its tunable electronic/magnetic properties are another important merit for applications in spintronic nanodevices.

4. Conclusion

In this study, we identified a stable 2D $CuCl_2$ crystal in the Cu−Cl binary systems using the PSO algorithm combined with DFT calculations. The $CuCl_2$ monolayer adopts a tetragonal *P*-4/*m*2 structure with $CuCl_4$-tetrahedrons as the basic unit, and exhibits auxetic behavior under a uniaxial strain with a high absolute value of NPR (0.40). Remarkably, the $CuCl_2$ monolayer exhibits intrinsic ferromagnetism with Curie temperature Tc of 47 K, which is associated with its Cu 3*d* configuration and the strong hybridization between Cu 3*d* states and Cl 3*p* states. Applying the biaxial strain and carrier doping, we theoretically examined and tuned their magnetic and electronic properties. When the compressive strain reaches 4% or the electron doping reaches 0.4 per f.u., the $CuCl_2$ monolayer can transfer from FM to NM state. Meanwhile, under a tensile strain of 4% or hole doping level of 0.6 per f.u., the $CuCl_2$ monolayer transforms from metal to half metal. All these findings suggest that the novel $CuCl_2$ monolayer is a promising candidate for future applications in spintronics and other nanodevices.

Author Information

Corresponding Authors

*E-mail: (Z. C.) zhongfangchen@gmail.com

*E-mail: (Y. C.) cyz@swjtu.edu.cn or cyz@swjtu.edu.cn

Notes

The authors declare no competing financial interest.

Acknowledgments

This work was supported in China by the Fundamental Research Funds for the Central Universities (2682020ZT110; 2018GF08), the Sichuan Science and Technology program (2020JY0314; 2017JY0056), and in USA by NASA (Grant Number 80NSSC19M0236) and NSF Center for the Advancement of Wearable Technologies (Grant 1849243).

References

1. N. D. Mermin and H. Wagner, *Phys. Rev. Lett.*, 1966, **17**, 1133-1136.
2. B. Huang, G. Clark, E. Navarro-Moratalla, D. R. Klein, R. Cheng, K. L. Seyler, D. Zhong, E. Schmidgall, M. A. McGuire, D. H. Cobden, W. Yao, D. Xiao, P. Jarillo-Herrero and X. Xu, *Nature*, 2017, **546**, 270-273.
3. C. Gong, L. Li, Z. Li, H. Ji, A. Stern, Y. Xia, T. Cao, W. Bao, C. Wang, Y. Wang, Z. Q. Qiu, R. J. Cava, S. G. Louie, J. Xia and X. Zhang, *Nature*, 2017, **546**, 265-269.
4. K. S. Burch, D. Mandrus and J.-G. Park, *Nature*, 2018, **563**, 47-52.
5. A. Soumyanarayanan, N. Reyren, A. Fert and C. Panagopoulos, *Nature*, 2016, **539**, 509-517.
6. Y. Zhou, Z. Wang, P. Yang, X. Zu, L. Yang, X. Sun and F. Gao, *ACS Nano*, 2012, **6**, 9727-9736.
7. W. S. Yun and J. D. Lee, *J. Phys. Chem. C.*, 2015, **119**, 2822-2827.
8. T. Cao, Z. Li and S. G. Louie, *Phys. Rev. Lett.*, 2015, **114**, 236602.
9. H. Peng, H. J. Xiang, S.-H. Wei, S.-S. Li, J.-B. Xia and J. Li, *Phys. Rev. Lett.*, 2009, **102**, 017201.
10. N. Miao, B. Xu, N. C. Bristowe, J. Zhou and Z. Sun, *J. Am. Chem. Soc.*, 2017, **139**, 11125-11131.
11. H. González-Herrero, J. M. Gómez-Rodríguez, P. Mallet, M. Moaied, J. J. Palacios, C. Salgado, M. M. Ugeda, J.-Y. Veuillen, F. Yndurain and I. Brihuega, *Science*, 2016, **352**, 437.

12. P. Manchanda, A. Enders, D. J. Sellmyer and R. Skomski, *Phys. Rev. B.*, 2016, **94**, 104426.

13. S. Radhakrishnan, D. Das, A. Samanta, C. A. de los Reyes, L. Deng, L. B. Alemany, T. K. Weldeghiorghis, V. N. Khabashesku, V. Kochat, Z. Jin, P. M. Sudeep, A. A. Martí, C.-W. Chu, A. Roy, C. S. Tiwary, A. K. Singh and P. M. Ajayan, *Sci. Adv.*, 2017, **3**, e1700842.

14. L. Ao, H. Y. Xiao, X. Xiang, S. Li, K. Z. Liu, H. Huang and X. T. Zu, *Phys. Chem. Chem. Phys.*, 2015, **17**, 10737-10748.

15. W. S. Yun and J. D. Lee, *Phys. Chem. Chem. Phys.*, 2014, **16**, 8990-8996.

16. M. R. Norman, *Rep. Prog. Phys.*, 2016, **79**, 074502.

17. A. d. l. Torre, K. L. Seyler, L. Zhao, S. D. Matteo, M. S. Scheurer, Y. Li, B. Yu, M. Greven, S. Sachdev, M. R. Norman and D. Hsieh, *Nat. Phys.*, 2021, DOI: 10.1038/s41567-021-01210-6.

18. M. G. Banks, R. K. Kremer, C. Hoch, A. Simon, B. Ouladdiaf, J. M. Broto, H. Rakoto, C. Lee and M. H. Whangbo, *Phys. Rev. B.*, 2009, **80**, 024404.

19. P. Reinhardt, M. P. Habas, R. Dovesi, I. de P. R. Moreira and F. Illas, *Phys. Rev. B.*, 1999, **59**, 1016-1023.

20. B. Sachs, T. O. Wehling, K. S. Novoselov, A. I. Lichtenstein and M. I. Katsnelson, *Phys. Rev. B.*, 2013, **88**, 201402.

21. E. Torun, H. Sahin, S. K. Singh and F. M. Peeters, *Appl. Phys. Lett.*, 2015, **106**, 192404.

22. H. Y. Lv, W. J. Lu, X. Luo, X. B. Zhu and Y. P. Sun, *Phys. Rev. B.*, 2019, **99**, 134416.

23. L. Webster and J.-A. Yan, *Phys. Rev. B.*, 2018, **98**, 144411.

24. M. A. McGuire, *Crystals*, 2017, **7**, 121.

25. J. He, S. Ma, P. Lyu and P. Nachtigall, *J. Mater. Chem. C.*, 2016, **4**, 2518-2526.

26. Y. Gao, M. Wu and X. C. Zeng, *Nanoscale. Horiz.*, 2019, **4**, 1106-1112.

27. Y. Wang, J. Lv, L. Zhu and Y. Ma, *Phys. Rev. B.*, 2010, **82**, 094116.

28. Y. Wang, J. Lv, L. Zhu and Y. Ma, *Comput. Phys. Commun.*, 2012, **183**, 2063-2070.

29. P. Kong, J. Wang, H. Wang, Y. Ni, H. Wang, Y. Tang, H. Liu and Y. Chen, *Phys. Chem. Chem. Phys.*, 2021, **23**, 14671-14677.

30. M. Xu, S. Shao, B. Gao, J. Lv, Q. Li, Y. Wang, H. Wang, L. Zhang and Y. Ma, *ACS Appl. Mater. Interfaces.*, 2017, **9**, 7891-7896.

31. Y. Chen, Z. Lao, B. Sun, X. Feng, S. A. T. Redfern, H. Liu, J. Lv, H. Wang and Z. Chen, *ACS Materials Letters*, 2019, **1**, 375-382.

32. I. Harran, Y. Chen, H. Wang and Y. Ni, *CrystEngComm*, 2018, **20**, 3928-3935.

33. J. Lv, Y. Wang, L. Zhu and Y. Ma, *Phys. Rev. Lett.*, 2011, **106**, 015503.

34. X. Cai, Y. Chen, B. Sun, J. Chen, H. Wang, Y. Ni, L. Tao, H. Wang, S. Zhu, X. Li, Y. Wang, J. Lv, X. Feng, S. A. T. Redfern and Z. Chen, *Nanoscale*, 2019, **11**, 8260-8269.

35. S. Zheng, T. Yu, J. Lin, H. Lou, H. Xu and G. Yang, *J. Mater. Chem. A.*, 2019, **7**, 25665-25671.

36. J. Chen, B. Sun, X. Cai, H. Wang and Y. Chen, *Comput. Mater. Sci.*, 2021, **199**, 110727.

37. L. Zhang, C. Tang, C. Zhang, Y. Gu and A. Du, *J. Mater. Chem. C.*, 2021, **9**, 3155-3160.

38. L. Shao, X. Duan, Y. Li, F. Zeng, H. Ye and P. Ding, *Phys. Chem. Chem. Phys.*, 2021, **23**, 666-673.

39. S. Lu, W. Hu and X. Hu, *J. Mater. Chem. C.*, 2021, **9**, 1387-1395.

40. M. Dion, H. Rydberg, E. Schröder, D. C. Langreth and B. I. Lundqvist, *Phys. Rev. Lett.*, 2004, **92**, 246401.

41. G. Kresse and J. Furthmüller, *Phys. Rev. B.*, 1996, **54**, 11169-11186.

42. J. P. Perdew, K. Burke and M. Ernzerhof, *Phys. Rev. Lett.*, 1996, **77**, 3865-3868.

43. P. E. Blöchl, *Phys. Rev. B.*, 1994, **50**, 17953-17979.

44. G. Kresse and D. Joubert, *Phys. Rev. B.*, 1999, **59**, 1758-1775.

45. J. Heyd, G. E. Scuseria and M. Ernzerhof, *JCP.*, 2003, **118**, 8207-8215.

46. H. J. Monkhorst and J. D. Pack, *Phys. Rev. B.*, 1976, **13**, 5188-5192.

47. A. Togo, F. Oba and I. Tanaka, *Phys. Rev. B.*, 2008, **78**, 134106.

48. G. J. Martyna, M. L. Klein and M. Tuckerman, *JCP.*, 1992, **97**, 2635-2643.

49. M. Kan, S. Adhikari and Q. Sun, *Phys. Chem. Chem. Phys.*, 2014, **16**, 4990-4994.

50. M. Kan, J. Zhou, Q. Sun, Y. Kawazoe and P. Jena, *J. Phys. Chem. Lett.*, 2013, **4**, 3382-3386.

51. L. Liu, X. Ren, J. Xie, B. Cheng, W. Liu, T. An, H. Qin and J. Hu, *Appl. Surf. Sci.*, 2019, **480**, 300-307.

52. Z. Gao, X. Dong, N. Li and J. Ren, *Nano. Lett.*, 2017, **17**, 772-777.

53. R. C. Cooper, C. Lee, C. A. Marianetti, X. Wei, J. Hone and J. W. Kysar, *Phys. Rev. B.*, 2013, **87**, 035423.

54. K. H. Michel and B. Verberck, *Phys. Rev. B.*, 2009, **80**, 224301.

55. H. Wang, X. Li, P. Li and J. Yang, *Nanoscale*, 2017, **9**, 850-855.

56. R. Peng, Y. Ma, Z. He, B. Huang, L. Kou and Y. Dai, *Nano. Lett.*, 2019, **19**, 1227-1233.

57. D. Wu, S. Wang, S. Zhang, J. Yuan, B. Yang and H. Chen, *Phys. Chem. Chem. Phys.*, 2018, **20**, 18924-18930.

58. B. Liu, M. Niu, J. Fu, Z. Xi, M. Lei and R. Quhe, *Phys. Rev. M.*, 2019, **3**, 054002.

59. S. Shen, Y. Ma, H. Wang, B. Huang and Y. Dai, *ACS Appl. Mater. Interfaces.*, 2019, **11**, 31793-31798.

60. A. N. Kocharian, G. W. Fernando, K. Palandage and J. W. Davenport, *Phys. Rev. B.*, 2008, **78**, 075431.

61. A. N. Kocharian, G. W. Fernando, K. Palandage and J. W. Davenport, *Phys. Rev. B.*, 2006, **74**, 024511.

62. S. Zheng, C. Huang, T. Yu, M. Xu, S. Zhang, H. Xu, Y. Liu, E. Kan, Y. Wang and G. Yang, *J. Phys. Chem. Lett.*, 2019, **10**, 2733-2738.

63. Y. Ran, M. Hermele, P. A. Lee and X.-G. Wen, *Phys. Rev. Lett.*, 2007, **98**, 117205.

64. X. Hu, Y. Zhao, X. Shen, A. V. Krasheninnikov, Z. Chen and L. Sun, *ACS Appl. Mater. Interfaces.*, 2020, **12**, 26367-26373.

65. X. Zhang, B. Wang, Y. Guo, Y. Zhang, Y. Chen and J. Wang, *Nanoscale. Horiz.*, 2019, **4**, 859-866.

66. X. Xu, Y. Ma, T. Zhang, C. Lei, B. Huang and Y. Dai, *Nanoscale. Horiz.*, 2020, **5**, 1386-1393.

67. N. Liu, S. Zhou and J. Zhao, *Phys. Rev. M.*, 2020, **4**, 094003.

68. J. M. D. Coey, M. Venkatesan and C. B. Fitzgerald, *Nat. Mater.*, 2005, **4**, 173-179.

69. H.-X. Deng, J. Li, S.-S. Li, J.-B. Xia, A. Walsh and S.-H. Wei, *Appl. Phys. Lett.*, 2010, **96**, 162508.

70. A. Walsh, J. L. F. Da Silva and S.-H. Wei, *Phys. Rev. Lett.*, 2008, **100**, 256401.

71. R. Albaridy, A. Manchon and U. Schwingenschlögl, *J. Phys. Condens. Matter.*, 2020, **32**, 355702.

72. H. L. Zhuang, P. R. C. Kent and R. G. Hennig, *Phys. Rev. B.*, 2016, **93**, 134407.

73. E. C. Stoner, *Proc. Roy. Soc. Lond. Math. Phys. Sci.*, 1939, **169**, 339-371.